

# Preparation of mesoporous TiO<sub>2</sub> nanomaterials doped with rare earth ions (La<sup>3+</sup>, Sm<sup>3+</sup>, Nd<sup>3+</sup>, Gd<sup>3+</sup>) and its application in the photodegradation of unsymmetrical dimethylhydrazine wastewater

Yizhi Zeng and Xianghong Ren\*

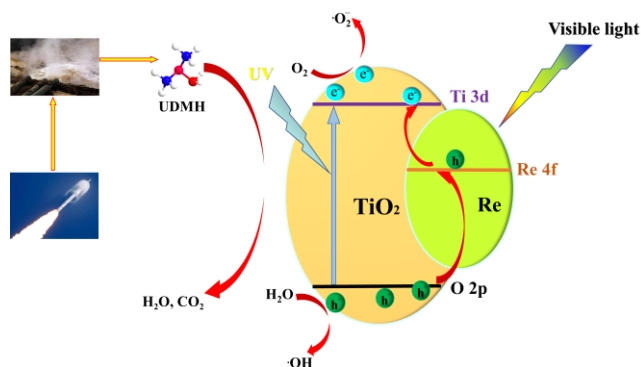
Xi'an Research Inst. of Hi-Tech, Xi'an 710025, China

Received: 03/08/2023, Accepted: 15/08/2023, Available online: 07/09/2023

\*to whom all correspondence should be addressed: e-mail: renxh701@163.com

<https://doi.org/10.30955/gnj.005280>

## Graphical abstract



## Abstract

Unsymmetrical dimethylhydrazine (UDMH) and its by-products cause serious damage to human health. In this paper, Re<sup>3+</sup>-doped mesoporous TiO<sub>2</sub> were synthesized for the photodegradation of UDMH. The structure, morphology and optical properties of photocatalyst were extensively characterized. The photocatalytic degradation was significantly enhanced, and 2%Nd-TiO<sub>2</sub> showed the most excellent photocatalytic degradation performance with 93.3% degradation rate of UDMH. NDMA and FDMH were gradually and completely degraded. ·O<sub>2</sub><sup>-</sup> and ·OH played an important role in the photocatalytic degradation of UDMH. The work provided an effective method for the degradation of UDMH wastewater.

**Keywords:** mesoporous TiO<sub>2</sub>, degradation, unsymmetrical dimethylhydrazine

## 1. Introduction

UDMH has been widely used as a high-energy liquid rocket fuel for missile weapons and aerospace applications because of its high specific impulse, low cost and easy storage. (Liu *et al.*, 2012) In the process of space launch, engine testing, fuel storage and transportation, a large amount of UDMH exhaust gas and waste liquid will be generated, which is prone to cancer and genetic mutation. (Carlsen *et al.*, 2009) The transformation products of

UDMH such as nitrosodimethylamine (NDMA) and metahydrazone (FDMH) are highly carcinogenic [Sgroi *et al.*, 2018], Therefore, it is of great practical significance to study the degradation and mineralization methods of UDMH. Traditional treatment methods of UDMH mainly include physical treatment, chemical treatment and biological treatment. Traditional physical treatment methods such as activated carbon adsorption and ion exchange can remove UDMH from wastewater smoothly, but activated carbon and ion exchange resin cannot be regenerated and recycled, which is easy to cause secondary pollution. (FleMing *et al.*, 1996) Chemical treatment methods such as H<sub>2</sub>O<sub>2</sub>/O<sub>3</sub>/UV degradation of UDMH in wastewater (Ismagilov *et al.*, 2002). Such methods are costly, energy intensive, and require MnO<sub>2</sub> and other substances to degrade the excess H<sub>2</sub>O<sub>2</sub> in the experiment, and O<sub>3</sub> will corrode the experimental equipment. Biological treatment methods mainly use aquatic plant absorption method and microbial degradation treatment, the treatment cycle is long and slow, and it is difficult to deal with large-scale high concentration of UDMH wastewater, and the above traditional methods all have certain defects.

Photocatalysis is a sustainable oxidation technology that directly uses solar energy and is an effective solution for degrading pollutants in water bodies (Rueda-Marquez *et al.*, 2020). TiO<sub>2</sub> photocatalysts are green and economical, highly active and non-selective in the degradation of water pollutants (Rashid *et al.*, 2023) which can mineralize potential pollutants into non-polluting substances, and is a hot spot for photocatalyst research (Gopinath *et al.*, 2020, Rahman *et al.*, 2023, Malik *et al.*, n.d.). However, the currently prepared TiO<sub>2</sub> photocatalytic materials generally have a wide band gap energy (E<sub>g</sub>, 3.0~3.2eV) responding to UV light only, with only 4%-5% of the available solar energy, limited use in visible light (400 nm < λ < 700 nm), and high photogenerated electron and hole complexation rates with low catalytic efficiency (Byrne *et al.*, 2018). It is found that doping can extend the spectral response range and reduce the complexation rate of electron-hole pairs, thus

improving the photocatalytic performance (Paradisi *et al.*, 2023, Liang *et al.*, 2023, Escamilla-Mejia *et al.*, 2023). Rare earth metals have high energy levels because of the unfilled 4f shell layers or empty 5d orbitals, and the energy levels of 4f, 5d, and 6s electrons are closely (Lee *et al.*, 2013), exhibiting unique properties and functions. It was reported (Wang *et al.*, 2011) that the doping of rare earth elements can effectively capture photogenerated electrons and prevent the recombination of photogenerated electrons and holes, which can improve the photocurrent conversion efficiency in the light of 300~400 nm. The absorption sidebands displayed a redshift, improved the utilization of visible light, and greatly improved the photocatalytic efficiency. Rare earth metal doping has now been widely used in the modification of photocatalysis (Zhao and Liu, 2008; Saif *et al.*, 2014; El-Bahy *et al.*, 2009), such as Eu-doped TiO<sub>2</sub> (Juan *et al.*, 2022), La-doped TiO<sub>2</sub> (Huang *et al.*, 2017), Nd-doped TiO<sub>2</sub> (Wang *et al.*, 2019), Er-doped TiO<sub>2</sub> (Chen *et al.*, 2022).

The preparation of TiO<sub>2</sub> nanomaterials with mesoporous structure is an effective way to enhance photocatalytic activity. Its large specific surface area and well-developed pore structure can facilitate the adsorption of reactants and the absorption of light energy, and it can generate more active reaction centers, thus improving photocatalytic activity (Hou *et al.*, 2020). There are various synthetic methods such as hydrothermal method, template method and sol-gel method to prepare mesoporous TiO<sub>2</sub> nanomaterials, however, it is still challenging to prepare mesoporous TiO<sub>2</sub> nanomaterials with high specific surface area and high crystallinity because the grain growth may lead to collapse of mesoporous structure.

In this paper, Re<sup>3+</sup>(La<sup>3+</sup>, Sm<sup>3+</sup>, Nd<sup>3+</sup>, Gd<sup>3+</sup>)-doped mesoporous titanium dioxide nanopowder were synthesized using a low energy consumption and low pollution hydrothermal method with simple organic reagents and inorganic acids. The effects of rare earth ion doping on the crystal structure, surface chemical state, morphology, optical properties and the effects of rare earth ion doping on the crystal structure, surface chemical state, morphology, optical properties and activity of photocatalytic degradation of UDMH were investigated. The mechanism of the photocatalytic process was inferred by free radical capture experiments and EPR analysis.

## 2. Experiment

### 2.1. Materials and reagents

UDMH, (98%), NDMA(>98%), O<sub>2</sub>si, FDMH(>98%), Aladdin Chemicals, Tetrabutyl titanate, Aladdin Chemicals, Inc. (>99%), HCl (AR), HNO<sub>3</sub> (AR), NaOH (AR), Xi'an Mipu Chemical Reagent Co., LTD., anhydrous ethanol (AR) Tianjin Hengxing Chemical Reagent Co., LTD., La<sub>2</sub>O<sub>3</sub>, Sm<sub>2</sub>O<sub>3</sub>, Nd<sub>2</sub>O<sub>3</sub>, Gd<sub>2</sub>O<sub>3</sub>, Aladdin Chemical Company 99.99%), isopropyl alcohol, p-benzoquinone, Disodium EDTA, Carbon Tetrachloride, Aladdin Chemicals Co., LTD. (>99.99%), deionized water, laboratory homemade. all reagents are analytical grade reagents, no further treatment is required when used.

### 2.2. Preparation of photocatalyst

As shown in Figure 1, the rare-earth modified mesoporous TiO<sub>2</sub> nanoparticles were synthesized by a one-step hydrothermal method. 15ml of tetrabutyl titanate was added dropwise to 20 ml of anhydrous ethanol with vigorous stirring for 60 min to obtain a light-yellow solution A. A certain concentration of HCl solution was added dropwise to solution A to obtain mixed solution B. A certain amount of lanthanide oxide was weighed and dissolved in HNO<sub>3</sub> to prepare 100ml of 50mM Re(NO)<sub>3</sub> solution was set aside, add different volumes of 50mM Re(NO)<sub>3</sub> solution drop by drop in solution B, stirring for 30min. to ensure that the material ratio of rare earth Re<sup>3+</sup> to TiO<sub>2</sub> was 0.5%, 1%, 2% and 3%, respectively, slowly added NaOH solution drop by drop, adjusted the pH to about 7 and stirred for 1h, in turn the suspension was transferred to a 100ml autoclave. reacting at 150°C for 24h. And then the supernatant was decanted after it cooled naturally to room temperature, centrifuged, rinsed with deionized water and anhydrous ethanol. To the sample TiO<sub>2</sub> was obtained by by filtration, drying and grinding, 0.5%Re<sup>3+</sup>-TiO<sub>2</sub>, 1%Re<sup>3+</sup>-TiO<sub>2</sub>, 2%Re<sup>3+</sup>-TiO<sub>2</sub>, 3%Re<sup>3+</sup>-TiO<sub>2</sub> are simply noted as TiO<sub>2</sub>, 0.5%Re-TiO<sub>2</sub>, 1%Re-TiO<sub>2</sub>, 2%Re-TiO<sub>2</sub>, 3%Re-TiO<sub>2</sub>.

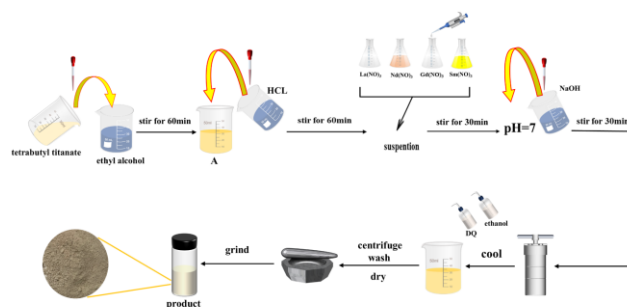


**Figure 1.** The process diagram of materials preparation

### 2.3. Characterization

The physical composition and crystal were examined by X-ray diffractometer (XRD, bruker D8 advanced, Germany) with the following operating parameters: Cu target, K $\alpha$  rays,  $\lambda=0.15401$  nm, target voltage 40KV, scanning range 5°~90°, scanning speed 5°/min, FT-IR spectroscopy (FT-IR, bruker VERTEX 70, Germany) to measure the FT-IR spectra of the samples in the range of 450 cm<sup>-1</sup>~4000 cm<sup>-1</sup>, KBr was used as diluent, and the elemental composition of the material surface was determined by X-ray photoelectron spectrometer (XPS, AXIS ULTRADLD, UK) and analyzed for its chemical valence state, the C 1s peak at 284.8 eV for calibration of binding energy. The surface morphology of the material was observed by a cold emission scanning electron microscope (FESEM, Gemini, Germany) equipped with EDS at a high-speed voltage of 15 kV, and the elemental composition and relative content of the material were determined by an energy spectrometer (EDS). The microscopic morphology and crystal structure of the materials were further observed by a high-resolution transmission electron microscope (HRTEM, JEM-2100F, Japan), and the crystalline spacing was analyzed, and the absorption properties of the UV-Vis diffuse reflectance spectra were tested by a UV-Vis spectrometer (UV-Vis DRS, Ocean Optics SB650, USA). PL steady-state spectra with excitation wavelength of 325 nm, Raman spectra were

obtained by nanoraman spectrometer (Naman, HORIBA JY HR-800, France) under 532 nm excitation, the specific surface area of the material was measured by specific surface area and porosity analyzer (JW-BK300, China), and the pore size distribution was calculated by BJH method, and the pore size distribution was calculated by electron paramagnetic resonance spectrometer (EPR, Bruker A300, Germany) to collect electron paramagnetic resonance spectra, detect and analyze free radicals, photoelectrochemical measurements were performed at an electrochemical workstation (Priston P4000, USA) by the chronocurrent method, FDMH, NDMA by high performance liquid chromatography (HPLC, Ultimate 3000, USA)

#### 2.4. Analysis method

The photocatalytic activity of the catalysts was evaluated by decomposing the UDMH under a 350W xenon lamp, using a CEL-LAB500E 350W xenon lamp with AM 1.5 filter to simulate sunlight as the light source (100 mW/cm<sup>2</sup>). The photocatalyst was stirred for 30 min to ensure the adsorption-desorption equilibrium, and the suspension was centrifuged to measure the absorbance A value of the upper clear layer.

The degradation efficiency R, mineralization efficiency and reaction kinetics of UDMH were used to evaluate the photocatalytic performance. The formula is as follows:

$$R = (C_0 - C_t) / C_0 \quad (1)$$

Where: C<sub>0</sub> is the initial concentration of UDMH, mg/L; C<sub>t</sub> is the concentration of UDMH in the wastewater at the time of photocatalytic reaction t, mg/L. In addition, the general photocatalyst degradation of organic pollutants is a pseudo primary kinetic reaction with the following equation:

$$\ln \frac{C_0}{C_t} = kt \quad (2)$$

Where: k is the first-order kinetic reaction rate constant, h<sup>-1</sup> or min<sup>-1</sup>; t is the time of photocatalytic degradation of UDMH.

$$\text{Mineralization rate}(\%) = \frac{\text{TOC}_0 - \text{TOC}_t}{\text{TOC}_0} \times 100\% \quad (3)$$

Where: TOC<sub>0</sub> and TOC<sub>t</sub> were the concentration of total organic carbon (TOC) at the initial and t.

The method used for the determination of UDMH in the experiment was the spectrophotometric method of sodium aminoferricyanide in GB/T 14376-1993 (Zhang *et al.*, 2023), with UV-vis spectrometer (721, Shanghai Instrument Analysis Factory, China), UDMH reacted with sodium aminocyanide to form a red complex with a maximum absorption wavelength of 500 nm, and the concentration of UDMH was determined by the principle that the color depth of the red complex is proportional to the content of UDMH (Zhou *et al.*, 2020). Further assessment of mineralization of UDMH wastewater by means of a TOC analyzer (Elementar Analysensysteme GmbH, Germany).

#### 2.5. Photoelectrochemical performance analysis

Prior to film coating, the transparent indium tin oxide (ITO) glass substrates were spin-coated a layer of conductive adhesive. Then, they were coated with the previous solution by the quantitative flow continuation film forming method. The as-prepared photoelectrodes were used as working electrodes; Ag/AgCl and Pt foil were used as reference and counter electrodes, respectively. Na<sub>2</sub>SO<sub>4</sub> aqueous solution (1.0 M) was used as the electrolyte. and the photoelectrochemical performance was tested by chrono-current, and the current density was measured under light and dark conditions, and the separation efficiency was judged by the photocurrent changes of photoelectrons. Free radical capture experiment

According to the basic principle of photocatalysis, the degradation process of organic matter mainly consists of direct oxidation of organic pollutants by photogenerated pairs, or the reaction with surface adsorbed oxygen (O<sub>2</sub>) and H<sub>2</sub>O/OH<sup>-</sup> to generate superoxide radicals(O<sub>2</sub><sup>-</sup>) and hydroxyl radical (OH). In order to determine the mechanism of photocatalytic degradation of UDMH, different radical trapping agents were added to the photocatalytic degradation of UDMH, and the role of each radical in the photocatalytic degradation process was evaluated by verifying the type of reacting radicals, and this paper mainly used isopropyl alcohol, p-benzoquinone, disodium ethylenediaminetetraacetic acid (Na<sub>2</sub>EDTA), and carbon tetrachloride as capture agent of OH, ·O<sub>2</sub><sup>-</sup>, h<sup>+</sup> and e<sup>-</sup>. Set the addition concentration at 1 mM and analyze the effect of active species produced by different photocatalysts on the degradation of UDMH wastewater, using the UDMH wastewater degradation system with only the catalyst added as a blank reference, no trapping agent was added and other conditions were kept consistent (Alam *et al.*, 2018).

### 3. Results and discussions

#### 3.1. Structural analysis of photocatalysts

The crystal structure of the samples was studied by X-ray diffractometer (XRD). Figure 2 shows that the XRD spectra of pure TiO<sub>2</sub> and Re<sup>3+</sup>-doped TiO<sub>2</sub> are in basic agreement with the standard card of anatase phase TiO<sub>2</sub> (PDF:21-1272), the characteristic diffraction peaks of each crystal plane family in the spectra are sharp, and the material has good crystallization properties, The 2θ characteristic diffraction peaks at 25.3°, 37.5°, 48.2°, 55.1°, 62.9° correspond to the (101), (004), (200), (105), (204) crystallographic planes of anatase titanium dioxide crystals (Fan *et al.*, 2014). The diffraction peaks of Re<sup>3+</sup>-doping are not significantly different from those of pure TiO<sub>2</sub>, and the diffraction peaks of rare earth oxides do not appear after doping, indicating that the rare earth elements are uniformly dispersed in the TiO<sub>2</sub> phase after doping, and there is no independent phase (Hassan *et al.*, 2012). Considering the radii of Nd<sup>3+</sup> (0.100 nm), La<sup>3+</sup> (0.106 nm), Sm<sup>3+</sup> (0.096 nm), Gd<sup>3+</sup> (0.094 nm), which are much larger than the radius of Ti<sup>4+</sup> (0.068 nm), it is difficult for Re<sup>3+</sup> to directly enter the lattice of TiO<sub>2</sub> to replace Ti<sup>4+</sup> to form a stable solid solution, but it is uniformly dispersed in the form of clusters in TiO<sub>2</sub> nanoparticles or in the

interstices of the iron-oxygen octahedra of titanium dioxide (Nguyen-Phan *et al.*, 2009). In Figure 2 (b), although the different  $\text{Re}^{3+}$  doping process did not change the crystalline phase of  $\text{TiO}_2$ , the diffraction peak half-peak width gradually increased and intensity gradually decreased compared with the undoped sample, and (101) the crystalline surface shifted to a low angle, and in Figure 2 (a), when  $\text{Nd}^{3+}$  was doped, the doping ratio gradually increased, and the trend of peak broadening and dwarfing became more obvious, the different  $\text{Re}^{3+}$  doping inhibits the growth of titanium dioxide grains and causes grain refinement, and within a certain doping ratio, the trend of grain refinement is more obvious as the amount of  $\text{Re}^{3+}$  doping increases. The grain refinement can increase the specific surface area and enhance the oxidation ability of the photocatalyst through the quantum size effect, which will be beneficial to the non-homogeneous photocatalytic reaction.

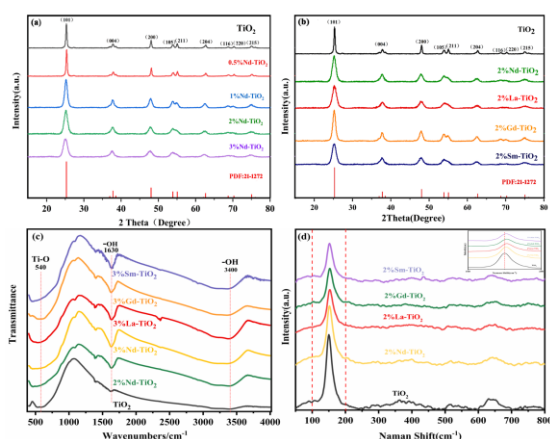


**Figure 2.** (a) XRD of pure  $\text{TiO}_2$  and  $\text{TiO}_2$  doped with different concentrations of  $\text{Nd}^{3+}$  (b) XRD of pure  $\text{TiO}_2$  and 2%  $\text{Re-TiO}_2$  ( $\text{Nd}^{3+}$ ,  $\text{La}^{3+}$ ,  $\text{Gd}^{3+}$ ,  $\text{Sm}^{3+}$ ) (c) FT-IR spectra of pure  $\text{TiO}_2$ , 2%  $\text{Nd-TiO}_2$  and 3%  $\text{Re-TiO}_2$  ( $\text{Nd}^{3+}$ ,  $\text{La}^{3+}$ ,  $\text{Gd}^{3+}$ ,  $\text{Sm}^{3+}$ ) (d) Raman spectra of pure  $\text{TiO}_2$  and 2%  $\text{Re-TiO}_2$  ( $\text{Nd}^{3+}$ ,  $\text{La}^{3+}$ ,  $\text{Gd}^{3+}$ ,  $\text{Sm}^{3+}$ )

The information of the chemical structure of the samples was further investigated by FT-IR test, and Figure 2 (c) shows that all samples showed three characteristic absorption peaks at  $540\text{ cm}^{-1}$ ,  $1630\text{ cm}^{-1}$ , and  $3400\text{ cm}^{-1}$ , which were attributed to the Ti-O stretching vibration in anatase  $\text{TiO}_2$ , the bending vibration of physisorbed water molecules -OH, and the stretching of surface -OH from water dissociation vibration, compared with pure  $\text{TiO}_2$ , the characteristic peak at  $1630\text{ cm}^{-1}$  is significantly enhanced after doping, and the peak of 3%  $\text{Nd-TiO}_2$  is stronger than that of 2%  $\text{Nd-TiO}_2$ , probably because after  $\text{Re}^{3+}$  doping,  $\text{Ti}^{4+}$  replaces  $\text{Re}^{3+}$  at the rare-earth oxide lattice interface and forms Ti-O-Re bond leading to lattice distortion, which increases the number of surface-OH, and at the same time the Ti-O characteristic peak is red-shifted. The  $3440\text{ cm}^{-1}$  characteristic absorption peak indicates that the photogenerated  $\text{h}^+$  generated by  $\text{TiO}_2$  after photoexcitation reacts with  $\text{H}_2\text{O}$  or  $\text{OH}^-$  to form  $\cdot\text{OH}$ . The enhancement of the peak at  $3440\text{ cm}^{-1}$  after doping indicates that the number of  $\cdot\text{OH}$  increases after doping, which is beneficial to the photocatalytic reaction activity, and this change may be due to the increase of specific surface area after  $\text{Re}^{3+}$  doping. The new characteristic peaks did not appear after

doping, and only some of the peaks were broadened and distorted, which is a change in the interaction forces between the groups only after doping, which corroborates with the XRD results.

The crystal structure and surface defects of the samples were further investigated by Raman tests.  $144\text{ cm}^{-1}(\text{E}_g)$ ,  $197\text{ cm}^{-1}(\text{E}_g)$ ,  $639\text{ cm}^{-1}(\text{E}_g)$ ,  $513\text{ cm}^{-1}(\text{A}_{1g})$ , and  $396\text{ cm}^{-1}(\text{B}_{1g})$  Raman vibrational peaks revealed the synthesis of anatase phase  $\text{TiO}_2$  (Kibasomba *et al.*, 2018). After  $\text{Re}^{3+}(\text{Nd}^{3+}, \text{La}^{3+}, \text{Gd}^{3+}, \text{Sm}^{3+})$  doping, The strongest peak at  $144\text{ cm}^{-1}(\text{E}_g)$  is obviously weakened, indicating that the particle size of  $\text{TiO}_2$  decreases with  $\text{Re}^{3+}$  doping, and the anatase phase  $\text{TiO}_2$  is a tetragonal crystal system, and the change of  $\text{E}_g$  vibrational peak in the tetragonal crystal system can directly prove the generation of oxygen vacancies (Salari *et al.*, 2011), The inset in the upper right corner of Figure 2 (d) shows the strongest peak of the  $\text{E}_g$  pattern for all samples, which is shifted toward the high wave number, indicating that more oxygen vacancies are generated in the doped titanium dioxide nanolattice structure, and the oxygen vacancies can act as electron capture traps to inhibit carrier recombination. In addition, the oxygen vacancies can also form transition energy levels between the conduction band and valence band, reducing the  $\text{E}_g$  and thus enhancing the visible light response, thus enhancing the photocatalytic activity (Jiang *et al.*, 2012).

### 3.2. Morphological analysis of photocatalysts

From Figure 3, it can be seen that the prepared photocatalysts are porous materials composed of inhomogeneous nanoparticles, and the phenomenon of particle agglomeration occurred in all samples. The prepared pure  $\text{TiO}_2$  is a group of irregular block structures with more fragments and cracks, with agglomerated morphology, and the particle size is about  $30\sim 40\text{ nm}$ . The doping of rare earth  $\text{Re}^{3+}$  ( $\text{Nd}^{3+}$ ,  $\text{Sm}^{3+}$ ,  $\text{Gd}^{3+}$ ,  $\text{La}^{3+}$ ) has an obvious inhibiting effect on the growth of  $\text{TiO}_2$ . The grain size of 1% $\text{Nd-TiO}_2$  is about  $15\sim 25\text{ nm}$ , 2% $\text{Nd-TiO}_2$  is about  $10\sim 20\text{ nm}$ , 3% $\text{Nd-TiO}_2$  is about  $10\sim 15\text{ nm}$ , with the increase of  $\text{Nd}^{3+}$  doping, the trend of grain refinement is more obvious, which is consistent with the xrd results and can be obtained from the increase of specific surface area in Table 1 corroborate (Parveen *et al.*, 2017). In order to determine the actual doping amount of  $\text{Re}^{3+}$  in  $\text{Nd-TiO}_2$ , EDS was used to test and analyze the content of 2%  $\text{Nd-TiO}_2$ . The peaks identified in the EDS plot corresponded to Ti, O, and Nd elements, and the mass ratio of Nd to  $\text{TiO}_2$  was calculated to be 2.03%, which was basically consistent with the expected doping amount, and the EDS results indicated the successful synthesis of 2% $\text{Nd-TiO}_2$  photocatalyst was successfully synthesized.



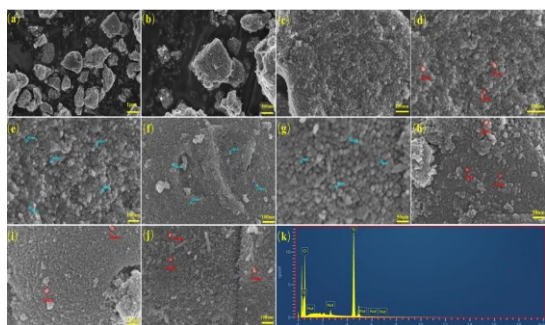


**Figure 3.** FESEM plots of (a) (b) (c) (d) pure TiO<sub>2</sub>, (e) 1%Nd-TiO<sub>2</sub>, (f) 2%Nd-TiO<sub>2</sub>, (g) 3%Nd-TiO<sub>2</sub> (h) 3% Sm-TiO<sub>2</sub>, (i) 2%Gd-TiO<sub>2</sub>, (j) 2%La-TiO<sub>2</sub> (k) EDS plots of 2%Nd-TiO<sub>2</sub>

HRTEM images can provide finer crystal internal results and analyze the crystalline surface spacing and defects. From Figure 4, The prepared samples have a particle size of about 10~30 nm, and the morphology is an aggregated state of nanoparticles, and the nanoparticles stack up to form porous channels similar to wormholes, which are randomly distributed between the nanoparticles and form a three-dimensional structure, which can increase the specific surface area of the catalyst, and then provide more catalytic reaction active sites, the prepared pure TiO<sub>2</sub> and Re<sup>3+</sup>-doped TiO<sub>2</sub> lattice stripes are clear, indicating good crystallinity, and the lattice stripe spacing of 0.352 nm, 0.351 nm, and 0.350 nm correspond to the (101) crystallographic plane of anatase TiO<sub>2</sub>, and because the radius of Re<sup>3+</sup> is larger than that of Ti<sup>4+</sup>, the lattice distortion caused by the doping of Re<sup>3+</sup>, locally (within the dashed box ) lattice stripe produces a slight expansion, and the generated impurity defects or oxygen vacancies can be used as traps for photogenerated electrons or holes to inhibit photogenerated electron-hole complexation and thus enhance photocatalytic activity.

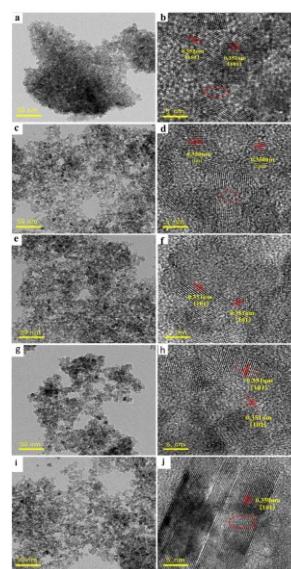


**Figure 4.** HRTEM images of (a), (b) pure TiO<sub>2</sub>, (c), (d) 2%La-TiO<sub>2</sub>, (e), (f) 2%Gd-TiO<sub>2</sub>, (g), (h) 2%Nd-TiO<sub>2</sub>, (i), (j) 2%Sm-TiO<sub>2</sub>

The physical and chemical conditions of the catalyst surface directly determine the catalytic reaction active sites and adsorption, which have important effects on the photocatalytic reaction. The specific surface area and pore size distribution of the samples were analyzed by BET method, and the nitrogen adsorption and desorption curves and pore size distribution curves are shown in Figure 5. The specific surface area and pore size (DP) data of the samples are included in Table 1. At lower relative pressures (P/P<sub>0</sub><0.4), the adsorption of the material is high, indicating the presence of mesoporous structure, and a type IV curve appears at relative pressures P/P<sub>0</sub>=0.4~0.8 with H<sub>4</sub> and H<sub>2</sub> hysteresis loops, indicating that the material is a typical mesoporous material (Thommes *et al.*, 2015), containing "ink bottle" interstitial pores. This is consistent with the results of the porous channels in the SEM photographs, where monolayer adsorption occurs mainly on the mesoporous pore walls at low relative pressures, with minimal micropore adsorption; at moderate relative pressures, adsorption increases rapidly and capillary coalescence occurs; and at high relative pressures, adsorption limitation occurs.

**Table 1.** BET specific surface area (SBET), pore volume and average pore size of the prepared samples

Sample	S <sub>BET</sub> (m <sup>2</sup> /g)	Pore volume (cm <sup>3</sup> /g)	Pore size (nm)	Sample	S <sub>BET</sub> (m <sup>2</sup> /g)	Pore volume (cm <sup>3</sup> /g)	Pore size (nm)
Pure TiO <sub>2</sub>	130.5	0.196	5.455	3%Gd-TiO <sub>2</sub>	172.4	0.237	4.323
3%Sm-TiO <sub>2</sub>	184.8	0.251	3.971	2%Gd-TiO <sub>2</sub>	155.4	0.215	4.378
2%Sm-TiO <sub>2</sub>	174.3	0.223	4.037	1%Gd-TiO <sub>2</sub>	142.2	0.203	4.613
1%Sm-TiO <sub>2</sub>	165.2	0.201	4.362	0.5%Gd-TiO <sub>2</sub>	133.4	0.196	4.939
0.5%Sm-TiO <sub>2</sub>	149.6	0.198	5.016	3%La-TiO <sub>2</sub>	163.7	0.218	5.155
3%Nd-TiO <sub>2</sub>	187.7	0.230	3.494	2%La-TiO <sub>2</sub>	151.1	0.205	5.246
2%Nd-TiO <sub>2</sub>	180.3	0.217	3.667	1%La-TiO <sub>2</sub>	145.5	0.199	5.363
1%Nd-TiO <sub>2</sub>	160.5	0.204	3.697	0.5%La-TiO <sub>2</sub>	139.3	0.197	5.433
0.5%Nd-TiO <sub>2</sub>	153.8	0.201	3.786				

The pore size distribution diagram shows that the pore size distribution of the prepared samples is all located in the narrow range of 2~10 nm, which indicates that the

intermediate pore distribution of the samples is concentrated and uniformly ordered. The specific surface area and pore volume of 3%Sm-TiO<sub>2</sub>, 3%Nd-TiO<sub>2</sub> and

2%Nd-TiO<sub>2</sub> are larger, which can expose more active sites in the photocatalytic process and thus enhance the photocatalytic performance.

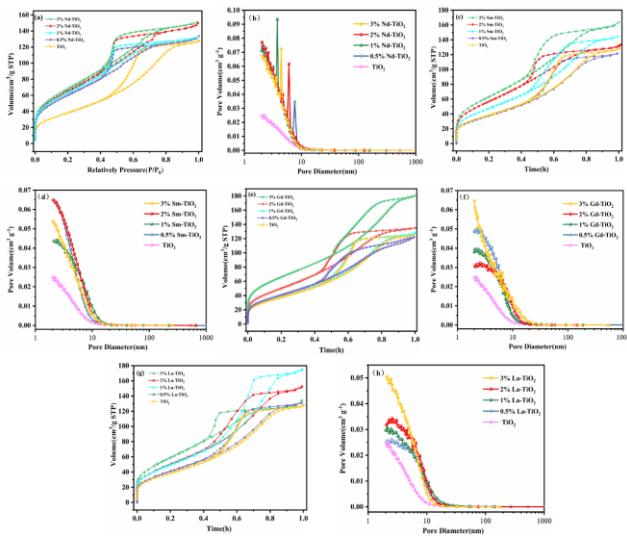


**Figure 5.** N<sub>2</sub> adsorption-desorption isotherms of (a) TiO<sub>2</sub> and Nd-TiO<sub>2</sub>, (c) pure TiO<sub>2</sub> and Sm-TiO<sub>2</sub>, (e) pure TiO<sub>2</sub> and Gd-TiO<sub>2</sub>, (g) pure TiO<sub>2</sub> and La-TiO<sub>2</sub>, pore size distribution curves of (b) TiO<sub>2</sub> and Nd-TiO<sub>2</sub>, (d) TiO<sub>2</sub> and Sm-TiO<sub>2</sub>, (f) TiO<sub>2</sub> and Gd-TiO<sub>2</sub>, (h) TiO<sub>2</sub> and La-TiO<sub>2</sub>.

### 3.3. Analysis of chemical composition of photocatalysts

The elemental nature of the surface layer of the photocatalyst was analyzed by XPS to further determine the presence state of each element, and the total spectra in Figure 6 (a), (b), (c) and (d) show that the materials all contain Ti, Re (Sm, Nd, Gd, La), O and C. Figure 7 (e), (f), (g) and (h) are the XPS spectra of Nd 3d, O 1s, Ti in 2%Nd-TiO<sub>2</sub> 2p and C 1s XPS spectra, the characteristic peaks of Nd are located at 983.4 eV and 1003.6 eV, respectively, which represent the bond energies of Nd 3d<sub>5/2</sub> and Nd 3d<sub>3/2</sub> (Yuvakkumar and Hong, 2015), The asymmetric peaks of O 1s appear in two separate peaks at binding energies 530.2eV and 532.4eV, respectively, indicating the existence of two different types of oxygen species on the surface after doping modification, where the strong peak at 530.2eV is the Ti-O<sub>lattice</sub> chemical bond formed between titanium and oxygen elements in the lattice, corresponding to the lattice oxygen species, and the weak peak at 532.4eV is the Ti-O<sub>surf</sub> chemical bond formed between titanium and oxygen elements on the surface of the catalyst, corresponding to the lattice oxygen species. elements on the catalyst surface, and the corresponding oxygen species are surface hydroxyl oxygen and oxygen vacancies (Xing *et al.*, 2013). The XPS peaks of Ti 2p at binding energies 458.4 eV and 464.1 eV belong to Ti 2p<sub>3/2</sub> and Ti 2p<sub>1/2</sub>, respectively, and the characteristic peaks of Ti 2p<sub>3/2</sub> and Ti 2p<sub>1/2</sub> in the Nd-modified catalysts are shifted towards lower binding energies compared to those of pure TiO<sub>2</sub> at binding energies 458.5 eV and 464.5 eV (Nair *et al.*, 2023), which indicates that the 2% Nd-TiO<sub>2</sub>, in addition to a large amount of Ti<sup>4+</sup>, there is also a small amount of Ti<sup>3+</sup>, and the radius of Nd<sup>3+</sup> (0.100 nm) is much larger than Ti<sup>4+</sup> (0.068 nm) and smaller than O (0.140 nm), so it is difficult for Nd<sup>3+</sup> to directly enter TiO<sub>2</sub> to replace Ti<sup>4+</sup>, but Ti<sup>4+</sup> may replace Nd<sup>3+</sup> at the rare-earth oxide lattice interface, which can form Ti-

O-Nd bond, because Ti<sup>4+</sup> is more electronegative than Nd<sup>3+</sup>, it is easy to get electrons and make its characteristic peak move to low binding energy, and part of Ti<sup>4+</sup> is reduced to Ti<sup>3+</sup> (Nguyen-Phan *et al.*, 2009). The formation of Ti<sup>3+</sup> and the oxygen vacancies on the catalyst surface facilitate the photocatalytic activity there is a clear splitting of the C 1s peak, with the strong peak at 284.8 eV being the XPS-calibrated C contamination, while the other two weaker binding energy peaks are formed by the carbon-containing material in the air absorbed by the sample.

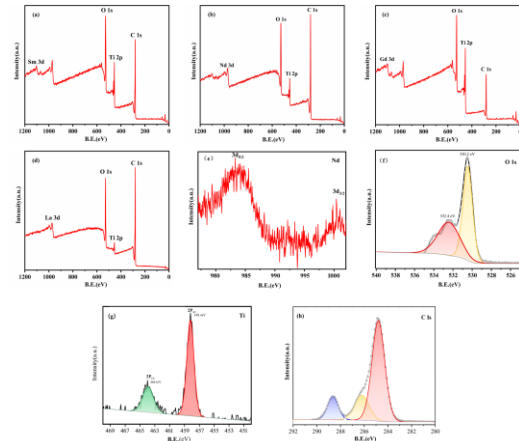


**Figure 6.** (a) Sm<sup>3+</sup>-doped TiO<sub>2</sub> photocatalyst XPS full spectrum; (b) Nd<sup>3+</sup>-doped TiO<sub>2</sub> photocatalyst XPS full spectrum; (c) Gd<sup>3+</sup>-doped TiO<sub>2</sub> photocatalyst XPS full spectrum; (d) XPS full spectrum of La<sup>3+</sup>-doped TiO<sub>2</sub> photocatalyst; (e) high-resolution X-ray photoelectron spectra of Nd 3d (f) O 1s (g) Ti 2p (h) C 1s;

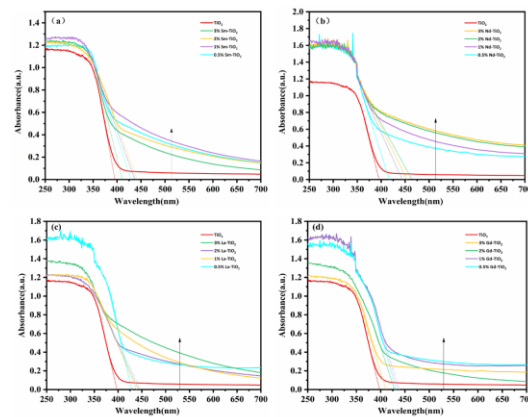


**Figure 7.** UV-vis of (a) TiO<sub>2</sub> and Sm<sup>3+</sup>-doped TiO<sub>2</sub> (b) TiO<sub>2</sub> and Nd<sup>3+</sup>-doped TiO<sub>2</sub> (c) TiO<sub>2</sub> and La<sup>3+</sup>-doped TiO<sub>2</sub>, (d) TiO<sub>2</sub> and Gd<sup>3+</sup>-doped TiO<sub>2</sub> in different concentrations.

### 3.4. Optical properties of photocatalysts

Figure 7 (a), (b), (c), (d) shows the UV-Vis DRS spectra of pure TiO<sub>2</sub> and Sm<sup>3+</sup>, Nd<sup>3+</sup>, La<sup>3+</sup> and Gd<sup>3+</sup> ion doping, the absorption spectra can be used to measure the absorption ability of the photocatalysts to different wavelengths of light, calculate the absorption sideband wavelengths of different photocatalysts, and use the Khan formula (Pal and Kryschi, 2016) to find the energy gap ( $E_g$ ) of the samples, as shown in Table 2.

**Table 2.** Absorption sidebands and E<sub>g</sub> of pure TiO<sub>2</sub> and different concentrations of Sm<sup>3+</sup>, Nd<sup>3+</sup>, Gd<sup>3+</sup> and La<sup>3+</sup> doped photocatalysts

Sample	λ/nm	E <sub>g</sub>	Sample	λ/nm	E <sub>g</sub>
Pure TiO <sub>2</sub>	394	3.15	3%Gd-TiO <sub>2</sub>	411	3.02
3%Sm-TiO <sub>2</sub>	410	3.02	2%Gd-TiO <sub>2</sub>	428	2.90
2%Sm-TiO <sub>2</sub>	440	2.81	1%Gd-TiO <sub>2</sub>	433	2.86
1%Sm-TiO <sub>2</sub>	437	2.84	0.5%Gd-TiO <sub>2</sub>	431	2.88
0.5%Sm-TiO <sub>2</sub>	428	2.89	3%La-TiO <sub>2</sub>	446	2.78
3%Nd-TiO <sub>2</sub>	456	2.72	2%La-TiO <sub>2</sub>	442	2.80
2%Nd-TiO <sub>2</sub>	468	2.64	1%La-TiO <sub>2</sub>	438	2.84
1%Nd-TiO <sub>2</sub>	441	2.82	0.5%La-TiO <sub>2</sub>	426	2.91
0.5%Nd-TiO <sub>2</sub>	420	2.95			

Compared with pure TiO<sub>2</sub>, the doping of Re<sup>3+</sup> (Sm<sup>3+</sup>, Nd<sup>3+</sup>, La<sup>3+</sup>, Gd<sup>3+</sup>) redshifts the absorption band edge of the photocatalyst and enhances the absorption effect in both UV and visible regions, and the E<sub>g</sub> of pure TiO<sub>2</sub> is 3.15 eV, which is very close to that reported in the literature (Juan *et al.*, 2022). The E<sub>g</sub> are narrowed after doping with Re<sup>3+</sup>, which can enhance the visible light response of the photocatalyst and thus the photocatalytic activity. The special 4f electron energy level structure of rare earth ions makes the energy values of the ground state and excited state close to each other, and when the 4f electron energy level jumps from the ground state to the excited state. It extends the light absorption wavelength of TiO<sub>2</sub> and enhances the visible light activity of the photocatalyst (Radha *et al.*, 2022). Another reason may be the formation of impurity energy levels between the conduction band and valence band of TiO<sub>2</sub> after the doping of rare earth ions, which changes the relative position of the valence band and conduction band, narrowing the E<sub>g</sub> and causing the absorption edge to be red-shifted (Borgarello *et al.*, 1982). The energy difference between the lowest excited state energy level and the ground state energy level in the 4f electron energy levels of different rare earth ions is different, resulting in differences in light absorption ability. 2% Nd-TiO<sub>2</sub> has the most significant light absorption ability in the visible wavelength band greater than 400 nm, and the E<sub>g</sub> of the sample is reduced to the greatest extent, with the absorption sideband red-shifted by 74 nm and the corresponding E<sub>g</sub> reduced by 0.51 eV. The above phenomenon may be related to the Nd 4f<sup>4</sup>6s<sup>2</sup> outer electron arrangement, because its outer electron arrangement does not contain d electrons, 4f<sup>4</sup> is easy to interact with O 2p orbitals and form impurity energy levels, which can make the photogenerated electrons jump to form photogenerated carriers in multiple steps at lower energy, improve the visible light response and thus enhance the photocatalytic activity.

3.5. Photogenerated carrier separation analysis

Stronger photoluminescence peak intensity means higher photogenerated carrier recombination rate and lower separation efficiency of photogenerated electrons from holes in photocatalysts (Kumaravel *et al.*, 2020). It can be seen in Figure 8 that the doping of Re<sup>3+</sup> did not change the spectral line shape of TiO<sub>2</sub>, indicating that the introduction of Re<sup>3+</sup> did not cause a new luminescence phenomenon,

but only affected the intensity of the PL spectrum, and the samples before and after the modification all showed obvious photogenic spectral peaks in the wavelength range of 350~400 nm.

In Figure 8 (a), the relative intensities of the photogenic spectral peaks are in the order of 3%Gd-TiO<sub>2</sub> > TiO<sub>2</sub> > 0.5%Gd-TiO<sub>2</sub> > 2%Gd-TiO<sub>2</sub> > 0.5%Nd-TiO<sub>2</sub> > 1%Gd-TiO<sub>2</sub> > 1%Nd-TiO<sub>2</sub> > 3%Nd-TiO<sub>2</sub> > 2%Nd-TiO<sub>2</sub>. It means that the separation efficiency of the photogenerated carriers is 3%Gd-TiO<sub>2</sub> < TiO<sub>2</sub> < 0.5%Gd-TiO<sub>2</sub> < 2%Gd-TiO<sub>2</sub> < 0.5%Nd-TiO<sub>2</sub> < 1%Gd-TiO<sub>2</sub> < 1%Nd-TiO<sub>2</sub> < 3%Nd-TiO<sub>2</sub> < 2%Nd-TiO<sub>2</sub>. In Figure 8 (b) the relative intensities of the emission spectra are in the order of 3%La-TiO<sub>2</sub> > 2%La-TiO<sub>2</sub> > TiO<sub>2</sub> > 0.5%La-TiO<sub>2</sub> > 0.5%Sm-TiO<sub>2</sub> > 1%La-TiO<sub>2</sub> > 3%Sm-TiO<sub>2</sub> > 1%Sm-TiO<sub>2</sub> > 2%Sm-TiO<sub>2</sub>, this means that the separation efficiency of the photogenerated carriers is 3%La-TiO<sub>2</sub> < 2%La-TiO<sub>2</sub> < TiO<sub>2</sub> < 0.5%La-TiO<sub>2</sub> < 0.5%Sm-TiO<sub>2</sub> < 1%La-TiO<sub>2</sub> < 3%Sm-TiO<sub>2</sub> < 1%Sm-TiO<sub>2</sub> < 2%Sm-TiO<sub>2</sub>. The above results show that doping with rare earth Re<sup>3+</sup> can help to reduce the complex of photogenerated electrons and enhance the photocatalytic activity of TiO<sub>2</sub>, which is because the introduction of Re<sup>3+</sup> can refine TiO<sub>2</sub> nanoparticles and increase the concentration of oxygen vacancies and defects (Nithyaa and Jaya, 2021). However, when the amount of doping exceeds the optimal ratio, the excess Re<sup>3+</sup> may become the electron complexation center, increasing the electron-hole complexation rate and reducing the photocatalytic activity.

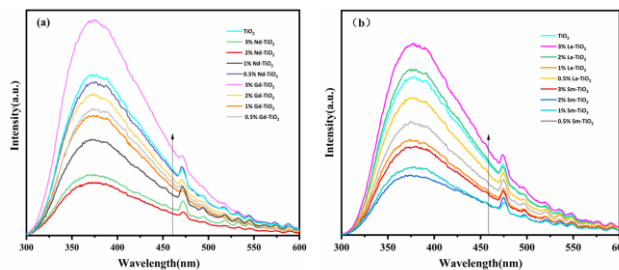


**Figure 8.** Photoluminescence spectra of (a) TiO<sub>2</sub>, different concentrations of Nd<sup>3+</sup>-doped TiO<sub>2</sub> and Gd<sup>3+</sup>-doped TiO<sub>2</sub> (b) TiO<sub>2</sub>, different concentrations of La<sup>3+</sup>-doped TiO<sub>2</sub> and Sm<sup>3+</sup>-doped TiO<sub>2</sub>. Generally, the higher the photocurrent, the more efficient the separation of photogenerated electrons from holes, which means the stronger the photocatalytic activity (Zhu *et al.*, 2020). According to the method of 2.5, pure TiO<sub>2</sub> and 1%Gd-TiO<sub>2</sub>, 1%La-TiO<sub>2</sub>, 2%Nd-TiO<sub>2</sub>, 2%Sm-TiO<sub>2</sub> photocatalysts were selected to prepare working electrodes, and the I-t curves were tested under the conditions of 20 s each of light and dark, as shown in Figure 9. All the samples had a fast light response, and constant photocurrent values could be obtained without delay in the light phase, and in the the current drops rapidly in the light-avoidance phase and maintains a stable value, indicating that the prepared electrode materials are sensitive to light response. It can be seen that the photocurrent response of pure TiO<sub>2</sub> is the weakest, from high to low, 2%Nd-TiO<sub>2</sub>, 2%Sm-TiO<sub>2</sub>, 1%La-TiO<sub>2</sub> and 1%Gd-TiO<sub>2</sub>. This result is consistent with the results of PL spectrum test and degradation test, which indicates that the degradation



performance of the photocatalyst is closely related to the carrier separation efficiency.

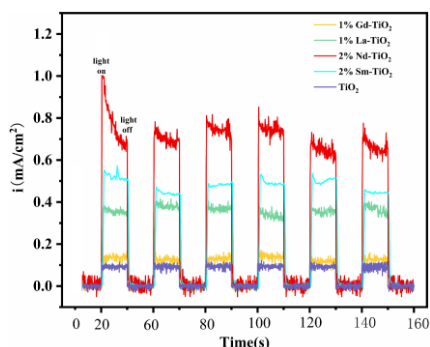


**Figure 9.** Photocurrent density plots of pure  $\text{TiO}_2$ , Gd- $\text{TiO}_2$ , La- $\text{TiO}_2$ , Nd- $\text{TiO}_2$ , Sm- $\text{TiO}_2$

### 3.6. Photocatalytic activity

#### 3.6.1. Degradation rate of UDMH

A 350W xenon lamp was used as a simulated light source to degrade UDMH wastewater under simulated sunlight to evaluate the catalytic degradation performance of the samples. The photocatalytic degradation of UDMH wastewater experiment was set up according to 2.4 by adding 3 g of catalyst to the reaction vessel and 50 ml of 100 mg/L UDMH wastewater. As shown in Figure 10 and Table 3, the natural degradation of 100 mg/L UDMH wastewater under simulated sunlight was almost negligible if no photocatalyst was added. The degradation rate of UDMH by the prepared pure  $\text{TiO}_2$  was 51.1%, and the photocatalytic activities of the samples doped with rare earths were all improved. The photocatalytic activities were closely related to the amount of rare earth doping. 3%Nd- $\text{TiO}_2$ , 2%Nd- $\text{TiO}_2$ , 1%Nd- $\text{TiO}_2$ , and 0.5%Nd- $\text{TiO}_2$  performed 84.5%, 93.3%, 82.1%, and 70.3% degradation rates, respectively. The doping amount was below 2%, with the increase of  $\text{Nd}^{3+}$  content, the number of traps in the catalyst that could capture photogenerated carriers increased, and the photogenerated electrons and holes could be separated effectively to make the photocatalytic activity enhanced, and the photocatalytic activity is enhanced, and when the n(Nd):n( $\text{TiO}_2$ ) is greater than 2%, the excess  $\text{Nd}^{3+}$  will form a large number of Ti-O-RE bonds, which will reduce the concentration of surface oxygen vacancies and defects, and will become the complex center of photogenerated carriers(Liang *et al.*, 2020), The photocatalytic activity is reduced, and from the kinetic analysis of the photocatalytic process. The degradation of UDMH followed a pseudo-kinetic first-order model, and the kinetic constants  $k$  values corresponding to the optimal doping amounts of pure  $\text{TiO}_2$  and Nd, Sm, La, and Gd under simulated visible light conditions were related as follows:

2%Nd- $\text{TiO}_2$ ( $k=0.25074\text{min}^{-1}$ ) > 2%Sm- $\text{TiO}_2$ ( $k=0.18512\text{min}^{-1}$ ) > 1%La- $\text{TiO}_2$ ( $k=0.14837\text{min}^{-1}$ ) > 1%Gd- $\text{TiO}_2$ ( $k=0.13913\text{min}^{-1}$ ) >  $\text{TiO}_2$ ( $k=0.06332\text{min}^{-1}$ ). It was obvious that 2%Nd- $\text{TiO}_2$  had the highest kinetic constant, which is consistent with the previous conclusion of photocatalytic activity. Since 2%Nd- $\text{TiO}_2$  exhibited the highest photocatalytic efficiency, all the following experiments were conducted to further investigate the photocatalytic performance. As shown in

Figure 11, to further evaluate the mineralization effect of 2%Nd- $\text{TiO}_2$  on UDMH, it was verified by TOC. The TOC degradation rate of UDMH wastewater could reach 84.8% under simulated sunlight irradiation.

**Table 3.** Degradation rates (DR%), reaction rate constants (K), and linear regression coefficients ( $R^2$ ) of pure  $\text{TiO}_2$ , Gd- $\text{TiO}_2$ , La- $\text{TiO}_2$ , Nd- $\text{TiO}_2$ , and Sm- $\text{TiO}_2$  for the degradation of UDMH

Samples	DR%	K( $\text{h}^{-1}$ )	$R^2$
Pure $\text{TiO}_2$	51.1	0.06332	0.99104
3%Sm- $\text{TiO}_2$	80.4	0.13755	0.98164
2%Sm- $\text{TiO}_2$	90.3	0.18512	0.96206
1%Sm- $\text{TiO}_2$	70.9	0.10395	0.99324
0.5%Sm- $\text{TiO}_2$	61.7	0.08493	0.99061
3%Nd- $\text{TiO}_2$	84.5	0.20067	0.97392
2%Nd- $\text{TiO}_2$	93.3	0.25074	0.97841
1%Nd- $\text{TiO}_2$	82.1	0.17508	0.98384
0.5%Nd- $\text{TiO}_2$	70.3	0.11279	0.96998
3%Gd- $\text{TiO}_2$	55.4	0.07484	0.98417
2%Gd- $\text{TiO}_2$	70.3	0.10463	0.98417
1%Gd- $\text{TiO}_2$	79.6	0.13913	0.97937
0.5%Gd- $\text{TiO}_2$	65.4	0.08498	0.98291
3%La- $\text{TiO}_2$	52.3	0.07019	0.99587
2% La- $\text{TiO}_2$	62.3	0.07348	0.99242
1% La- $\text{TiO}_2$	81.1	0.14837	0.97897
0.5% La- $\text{TiO}_2$	60.6	0.08381	0.99227

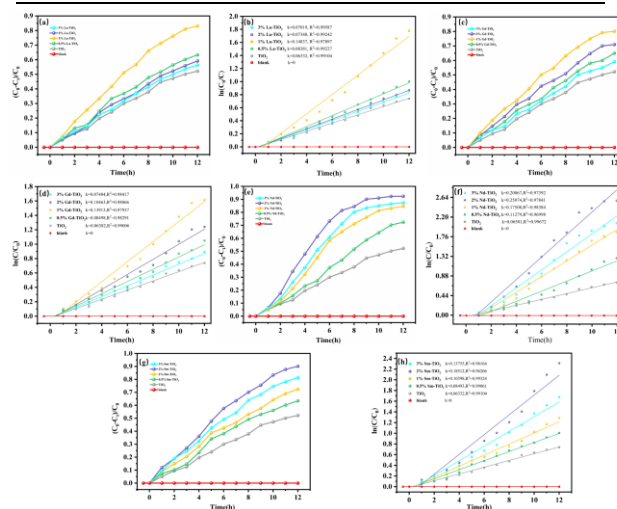


**Figure 10.** Photocatalytic degradation effect and kinetic linear fit of pure  $\text{TiO}_2$ , Gd- $\text{TiO}_2$ , La- $\text{TiO}_2$ , Nd- $\text{TiO}_2$ , Sm- $\text{TiO}_2$

#### 3.6.2. Degradation effect of FDMH and NDMA

The concentrations of NDMA and FDMH were tested according to the HPLC method previously studied by the group (Zhou *et al.*, 2021), The initial samples contained a small amount of NDMA and FDMH, and the trends of NDMA and FDMH were basically the same, first rapidly increasing and then slowly decreasing, and the rate of FDMH and NDMA generation by UDMH was greater than the rate of photocatalytic degradation of both at the initial stage, and both NDMA and FDMH reached the maximum concentration around 3h. At this time, the generation rate and degradation rate were almost equal, and the reaction gradually reached After that, the rate of photocatalytic degradation was greater than the rate of generation, and the concentration gradually decreased slowly, and the yield



of FDMH was significantly higher than that of NDMA, which might be because FDMH is an intermediate product of UDMH into NDMA, and it is easier to form NDMA from FDMH than from UDMH (Huang *et al.*, 2019), NDMA and FDMH were completely degraded at around 9h and 10h, respectively, indicating that UDMH could be completely mineralized.

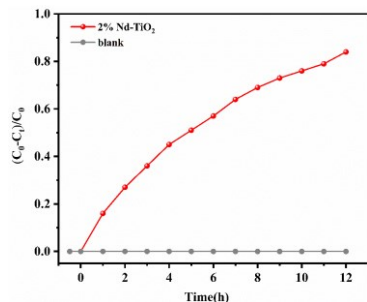


Figure 11. TOC detection during the degradation of UDMH wastewater

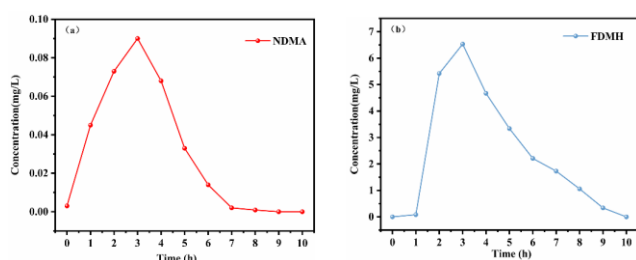


Figure 12. Degradation effect of 2%Nd-TiO<sub>2</sub> on NDMA and FDMH

### 3.6.3. Stability of photocatalysts

In addition to the photocatalytic activity, the stability of the photocatalyst is also an important evaluation criterion in the process of practical application. 50 ml of UDMH wastewater with a concentration of 50 mg/L was configured, and the recovery cycle experiment was conducted with 2%Nd-TiO<sub>2</sub> under the irradiation of 350 W xenon lamp, and the supernatant was decanted at the end of each cycle, centrifuged and rinsed with deionized water and anhydrous ethanol, dried at 70°C and then recirculated, as shown in Figure 12 (a) shows, the degradation efficiency of four cycles for UDMH was 94.55%, 89.36%, 87.86% and 85.7% in order to further confirm the stability of 2%Nd-TiO<sub>2</sub>, the 2%Nd-TiO<sub>2</sub> after UDMH cycle test was characterized by XRD and FTIR spectra, the results of XRD showed that the crystal structure of 2%Nd-TiO<sub>2</sub> did not significantly changed, and the FTIR results showed that the functional groups of 2%Nd-TiO<sub>2</sub> did not change significantly, and the photocatalytic activity of 2%Nd-TiO<sub>2</sub> was observed to decrease by 8.85% after four cycles, probably due to partial mass loss during centrifugation, washing and drying, rather than due to its passivation, and 2%Nd-TiO<sub>2</sub> has good stability as an efficient visible photocatalyst, but it also indicates that the powdered catalyst has the defects of tedious operation and easy loss in recoverability.

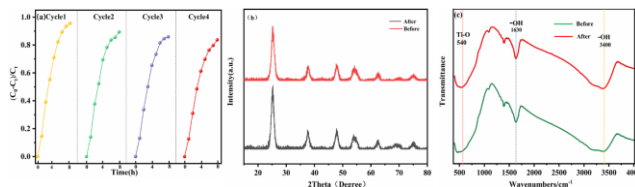


Figure 13. (a) Recycling test results of 2%Nd-TiO<sub>2</sub>, (b) XRD patterns before and after 2%Nd-TiO<sub>2</sub> test, (c) FTIR patterns before and after 2%Nd-TiO<sub>2</sub> test

### 3.7. Active substance identification

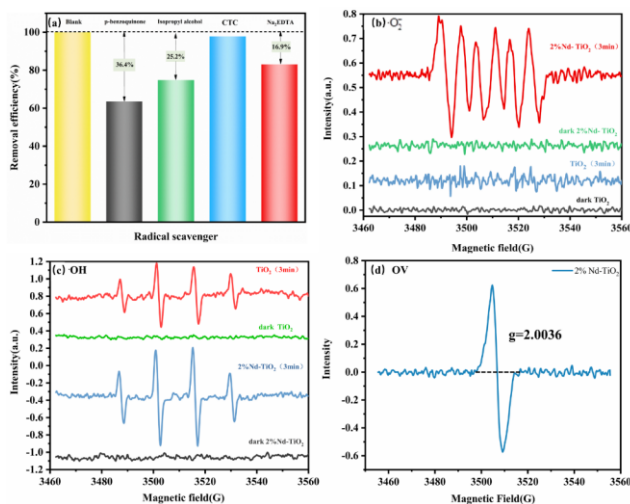


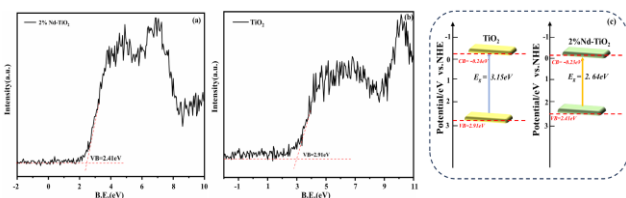
Figure 14. (a) active substance capture experiments based on visible light conditions to degrade UDMH, (b) EPR spectra of O<sub>2</sub><sup>-</sup> adducts captured under dark and visible light irradiation for 3 min, (c) EPR spectra of OH adducts captured under dark and visible light irradiation for 3 min, (d) EPR spectra of oxygen vacancies of 2%Nd-TiO<sub>2</sub>

The experimental conditions were designed as described in 2.6. 2%Nd-TiO<sub>2</sub> was selected as the photocatalyst, and the degradation rate of UDMH decreased in all groups after adding the trapping agent, indicating that, OH<sup>·</sup>, O<sub>2</sub><sup>-·</sup>, photogenerated h<sup>+</sup> and photogenerated e<sup>-</sup> participated in the photocatalytic degradation process, The values of the effect of isopropyl alcohol, p-benzoquinone, Na<sub>2</sub>EDTA, and carbon tetrachloride on the degradation efficiency of UDMH were 36.4 %, 25.2 %, 16.9 %, and 1.23 %, in that order. Therefore, the photocatalytic effect of active species on UDMH diminishes in the order of O<sub>2</sub><sup>-·</sup>>OH<sup>·</sup>> h<sup>+</sup>> e<sup>-</sup>. The effect of photogenerated e<sup>-</sup> on UDMH is small and can be ignored, O<sub>2</sub><sup>-·</sup> and OH<sup>·</sup> being the main active species. The EPR technique was used to identify and detect the ·O<sub>2</sub><sup>-</sup> and ·OH radicals, and 100 mM DMPO was used as the trapping agent. As shown in Figure 13 (a) and (b) under dark conditions, there was no obvious ·O<sub>2</sub><sup>-</sup> and ·OH radical signal in the EPR, and after 3 min of light, a four-peak EPR signal of 1:2:2:1 for DMPO-·OH was observed for both TiO<sub>2</sub> and 2%Nd-TiO<sub>2</sub>, and the DMPO-·O<sub>2</sub><sup>-</sup> six-peak signal, indicating that ·O<sub>2</sub><sup>-</sup> and ·OH radicals play a major role in this photocatalytic process, which was consistent with the results of the trapping experiments. 2%Nd-TiO<sub>2</sub> exhibited a stronger ·O<sub>2</sub><sup>-</sup> and ·OH signal compared to TiO<sub>2</sub>, indicating that the concentration of both ·O<sub>2</sub><sup>-</sup> and ·OH increases under visible light excitation after doping, g=2.0036 EPR signal of 2%Nd-TiO<sub>2</sub> in 13(d) indicated the presence of oxygen

vacancies in the lattice (Santara *et al.*, 2014), both the increase in the concentration of active species and the generation of oxygen vacancies were beneficial to enhance the photocatalytic activity.

### 3.8. Analysis of photocatalytic degradation mechanism

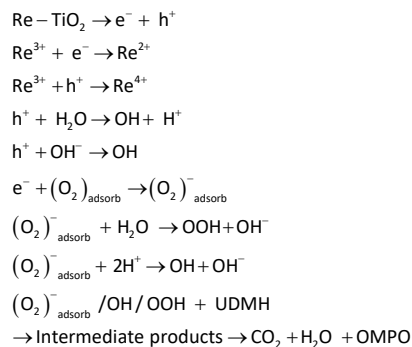
From the analysis of photocatalyst morphological structure, spectral absorption performance and photogenerated carrier separation, it had been confirmed that  $\text{Re}^{3+}$  doping improved the visible light response of  $\text{TiO}_2$  and increased the photogenerated electron yield, the  $E_g$  edge position of photocatalyst could be calculated by the formula  $E_{CB}=E_{VB}-E_g$ , the  $E_g$  structure of  $\text{TiO}_2$  and 2%  $\text{Nd-TiO}_2$  is shown in Figure 14. Combined with the spectral absorption performance and  $E_{VB}=2.91\text{eV}$  for pure  $\text{TiO}_2$  measured by XPS spectroscopy,  $E_g=3.15\text{eV}$  from UV-Vis DRS, and  $E_{CB}=-0.24\text{eV}$  calculated.  $E_{VB}=2.41\text{eV}$  for 2%  $\text{Nd-TiO}_2$ , UV-Vis DRS gives  $E_g=2.64\text{eV}$ , and  $E_{CB}=-0.23\text{eV}$  is calculated, the  $E_{CB}$  before and after doping are more negative than the oxidation potential of  $\text{O}_2/\cdot\text{O}_2^-$  ( $-0.046\text{eV}$  vs. NHE), and the photo-generated electrons ( $e^-$ ) can react with  $\text{O}_2$  to form  $\cdot\text{O}_2^-$ , and the  $E_{VB}$  before and after doping are larger than the reduction potential of  $\text{H}_2\text{O}/\cdot\text{OH}$  ( $2.4\text{eV}$  vs. NHE), so  $h^+$  can oxidize  $\text{H}_2\text{O}$  and  $\text{OH}^-$  directly to  $\cdot\text{OH}$  (Yang *et al.*, 2022).



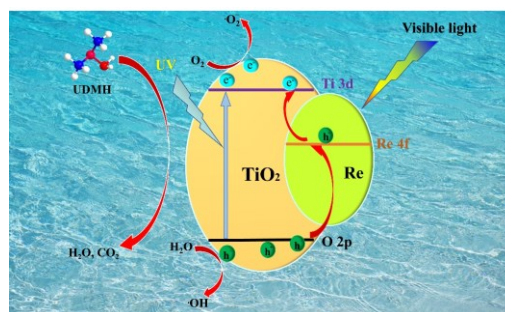
**Figure 15.** (a) VB-XPS spectrum of 2%Nd-TiO<sub>2</sub> (b) VB-XPS spectrum of TiO<sub>2</sub> (c) Schematic diagram of the energy band structure of 2%Nd-TiO<sub>2</sub> and TiO<sub>2</sub>

Figure 15 shows the mechanism diagram of rare earth single doped  $\text{TiO}_2$  photocatalytic degradation of UDMH, in pure  $\text{TiO}_2$ , under the excitation of UV light, the photocatalyst undergoes electron leap from O 2p to Ti 3d orbitals,  $\text{Re}^{3+}$  doping forms impurity energy level at the bottom of  $\text{TiO}_2$  conduction band, which reduces the  $E_g$  and extends the light absorption range to visible light region, under visible light irradiation, photogenerated electrons undergo O 2p to Nd 4f orbital electron leap. The electrons detached from the valence band are more likely to reach the conduction band, producing photogenerated electron-hole pairs, the unfilled 4f orbitals of  $\text{Re}^{3+}$  can capture photogenerated electrons, hindering the recombination of photogenerated electrons and holes, the resulting excited state of  $\text{Re}^{3+}$  can be oxidized with the photogenerated electrons produced in the valence band of  $\text{TiO}_2$ ,  $\text{Re}^{3+}$  captured photogenerated electrons are reduced to  $\text{Re}^{2+}$ , and The reduction reaction with the hole in the conduction band generates  $\text{Re}^{4+}$  (Liang *et al.*, 2020), Reaction of photogenerated electrons with  $\text{O}_2$  adsorbed on the surface of the receptor, forming  $(\text{O}_2)_{\text{adsorb}}^-$ .  $\cdot\text{OH}$  and  $\cdot\text{OOH}$  are formed by reacting with  $\text{H}_2\text{O}$  and  $h^+$ , while the cavity  $h^+$  reacts with

$\text{OH}^-$  or  $\text{H}_2\text{O}$  adsorbed on the surface to form  $\cdot\text{OH}$ , and it has been shown that  $\cdot\text{OOH}$ , which may be generated during the photocatalytic process, can participate in the UDMH reaction (Wang *et al.*, 1999; Liao and Gurol 1995), The generated  $(\text{O}_2)_{\text{adsorb}}^-$ ,  $\cdot\text{OH}$ ,  $\cdot\text{OOH}$  etc. are strongly oxidizing and can convert UDMH into  $\text{CO}_2$ ,  $\text{H}_2\text{O}$  and other small molecule products. The photocatalytic degradation of UDMH wastewater might involve the following processes:



It has also been reported (Li *et al.*, 2014) that  $\text{TiO}_2$  was able to produce  $\text{Ti}^{3+}$  under the effect of photoexcitation and is able to convert the lattice oxygen  $\text{O}_{\text{lattice}}$  inside the crystal to surface adsorbed oxygen  $(\text{O}_2)_{\text{adsorb}}$  after the transition state of O  $(\text{O}_2)_{\text{inter}}$ , which in turn can produce oxygen vacancies  $\text{O}_v$  with  $(\text{O}_2)_{\text{adsorb}}^-$ , the generated  $\text{Ti}^{3+}$  will produce a positive charge center, and to achieve charge balance, this center will adsorb photogenerated electrons, reducing the recombination efficiency of photogenerated carriers, can adsorb  $\text{OH}^-$ , and  $\text{OH}^-$  reacts with  $h^+$  to produce more  $\cdot\text{OH}$  to participate in the UDMH degradation reaction (El-Bahy *et al.*, 2009), and the generated oxygen vacancies can act as trapping sites for photoexcited electrons and promote the separation of electrons and holes (Ni *et al.*, 2021), It can form an intermediate energy band between the conduction band and valence band of  $\text{TiO}_2$  to reduce the  $E_g$  and enhance the response of visible light (Zhang *et al.*, 2011), thus improving the photocatalytic activity, and the formation of  $\text{Ti}^{3+}$  and oxygen vacancies on the catalyst surface are favorable to the photocatalytic activity.



**Figure 16.** Schematic diagram of the possible mechanism of degradation of UDMH by  $\text{Re-TiO}_2$  under visible light

## 4. Conclusion

In summary, a series of mesoporous  $\text{TiO}_2$  and  $\text{Re}^{3+}$  ( $\text{Sm}^{3+}$ ,  $\text{Nd}^{3+}$ ,  $\text{La}^{3+}$ ,  $\text{Gd}^{3+}$ )-doped  $\text{TiO}_2$  nanoparticles were prepared by a simple hydrothermal method, and the photocatalytic

activity of these samples was investigated by degradation of UDMH. The results showed that rare earth ion doping had a great influence on the photocatalytic activity, and 2%Nd-TiO<sub>2</sub> showed the highest photocatalytic efficiency. It could be attributed to its smaller grain size, larger specific surface area, enhanced visible light response after doping, and increased number of oxygen vacancies with minimal carrier complex probability. which made it show good degradation performance on UDMH through synergistic effect. The 2%Nd-TiO<sub>2</sub> did not show any significant activity loss after four cycles, indicating that it possesses excellent recyclable performance. In addition, according to radical capture experiments and EPR, the main active species in photocatalytic reactions were O<sub>2</sub><sup>-</sup> and ·OH.

## References

- Alam U., Khan A., Al D., Bahnermann D. and Muneer M. (2018). *RSC Advances*, **8**(31), 17582–17594.
- Borgarello E., Kiwi J., Gratzel M., Pelizzetti E. and Visca M. (1982). *Journal of the American Chemical Society*, **104**(11), 2996–3002.
- Byrne C., Subramanian G. and Pillai S.C. (2018). *Journal of Environmental Chemical Engineering*, **6**(3), 3531–3555.
- Carlsen L., Kenessov B.N., Batyrbekova S.Y., Kolumbaeva S.Z. and Shalakhmetova T.M. (2009). *Environmental Toxicology and Pharmacology*, **28**(3), 448–452.
- Chen J., Chen L., Wang X., Sun J., Chen A.Y. and Xie X.F. (2022). *Applications of Surface Science*, **596**, 153655.
- El-Bahy Z.M., Ismail A.A., Mohamed R.M.J. (2009). *Hazardous Materials*, **166**(1), 138–143.
- Escamilla-Mejia J.C., Hidalgo-Carrillo J., Martin-Gomez J., Lopez-Tenllado F.J., Estevez-Toledano R.C., Marinas. A. and Urbano F.J. (2023). *Catalysis Today*, **413**.
- Fan W.Q., Bai H.Y., Zhang G.H., Yan Y.S., Liu C.B. and Shi W.D. (2014). *Crystengcomm*, **16**(1), 116–122.
- FleMing E.C., PenningtFlemon J.C., Wachob B.G., Howe R.A. and Hill D.O. (1996). *Journal of Hazardous Materials*, **51**(1-3), 151–164.
- Gopinath K.P., Madhav N.V., Krishnan A., Malolan R. and Rangarajan G.J. (2020). *Environmental Management*, **270**, 110906.
- Hassan M.S., Amna T., Yang O.B., Kim H.C. and Khil M.S. (2012). *Ceramic Interfaces*, **38**(7), 5925–5930.
- Hou H.L., Shao G., Yang W.Y. and Wong W.Y. (2020). *Progress in Materials Science*, **113**.
- Huang D., Liu X.X., Wang X.J., Zuo C.S., Xie Z. and Gao X. (2019). *Chemical Physics*, **522**, 220–227.
- Huang Y., Cao J.J., Kang F., You S.J., Chang C.W. and Wang Y.F. (2017). *Aerosol and Air Quality Research*, **17**(10), 2555–2565.
- Ismagilov Z.R., Kerzhentsev M.A., Ismagilov I.Z., Sazonov V.A., Parmon V.N., Elizarova G.L., Pestunova O.P., Shandakov V.A., Zuev Y.L., Eryomin V.N., Pestereva N.V., Garin F. and Veringa. H.J. (2002). *Catalysis Today*, **75**(1-4), 277–285.
- Jiang X.D., Zhang Y.P., Jiang J., Rong Y.S., Wang Y.C., Wu Y.C., and Pan C.X. (2012). *Journal of Materials Chemistry C*, **116**(42), 22619–22624.
- Juan J.L.X., Maldonado C.S., Sanchez R.A.L. Diaz O.J.Z. Ronquillo M.R.R., Sandoval-Rangel L., Aguilar N. P., Delgado N.A.R and Martinez-Vargas D.X. (2022). *Catalysis Today*, **394**, 304–313.
- Kibasomba P.M., Dhlamini S., Maaza M., Maaza M., Liu C.P., Rashad M.M., Rayan.D.A. and Mwakikunga B.W. (2018). *Results in Physics*, **9**, 628–635.
- Kumaravel V., Rhatigan S., Mathew S., Michel M.C., Bartlett J., Nolan M., Hinder S.J., Gasco A., Ruiz-Palomar C. and Hermosilla D. (2020). *Journal of Physics: Materials*, **3**(2), 025008.
- Lee D.Y., Kim J.T., Park J.H., Kim Y.H., Lee I.K., Lee M. H., Kim B.Y. (2013). *Current Applied Physics*, **13**(7), 1301–1305.
- Li Y.F., Aschauer U., Chen J. and Selloni A. (2014). *Accounts of Chemical Research*, **47**(11), 3361–3368.
- Liang J.C., Wang J.Y., Song K.X., Wang X.F., Yu K.F. and Liang.C. (2020). *Journal of Rare Earths*, **38**(2), 148–156.
- Liang J.C., Wang J.Y., Yu K.F., Song K.X., Wang X.F., Liu W.P., Hau J.Z. and Liang C. (2020). *Chemical Physics*, **528**.
- Liang R.H., Hu Z.Z., Wu H.Z., Li S.S., Zhang X.Y., Arotiba O.A. and Zhou M.H. (2023). *Separation and Purification Technology*, **314**.
- Liao C.H. and Gurol M.D. (1995). *Environmental Science & Technology*, **29**(12), 3007–3014.
- Liu Z.J., Hu X.P., He Z. and Wu J.J. (2012) *Energies*, **5**(8), 3126–3136.
- Malik P., Sharma D. and Jajpura L. *Advanced Materials and Processes Technology*
- Nair P.R., Ramirez C.R.S., Pinilla M.A.G., Krishnan B., Avellaneda D.A., Pelaez R.F.C. and Shaji S. (2023). *Applied Surface Science*, **623**.
- Nguyen-Phan T.D, Song M.B., Kim E.J. and Shin E.W. (2009). *Microporous and Mesoporous Materials*, **119**(1-3), 290–298.
- Ni J.X., Wang W., Liu D.M., Zhu Q., Jia J.L., Tian J.Y., Li.Z.Y., Wang X. and Xing Z.P.(2021). *Journal of Hazardous Materials*, **408**.
- Nithyaa N. and Jaya N.V. (2021). *Applied Physics A: Materials Science & Processing*, **127**(1).
- Pal N.K. and Kryschi C. (2016). *Chemosphere*, **144**, 1655–1664.
- Paradisi E., Gualtieri M.L., Veronesi P., Dami V., Lorenzi G., Cioni A., Baldi G. and Leonelli C. (2023). *Advanced Materials and Processes Technology*, **6**(7), 5448–5459.
- Parveen B., Hassan M., Atiq S., Riaz S., Naseem S. and Toseef M.A. (2017). *Progress in Natural Science*, **27**(3), 303–310.
- Radha E., Komaraiah D., Sayanna R. and Sivakumar J. (2022). *Journal of Luminescence*, **244**.
- Rahman K.H., Kar A.K., Chen K.C. and Chen C.J. (2023). *Nanotechnology*, **34**(24).
- Rashid J., Bhatti T.T., Hassan M., Barakat M.A., Kumar R. and Xu M. (2023). *Fuel*, **346**.
- Rueda-Marquez J.J., Levchuk I., Ibanez P.F. and Sillanpaa M.J. (2020). *Cleaner Production Letters*, **258**.
- Saif M., Aboul-Fotouh S.M.K., El-Molla S.A., Ibrahim M.M. and Ismail L.F.M. (2014). *Spectrochimica Acta Part A: Molecular and Biomolecular Spectroscopy*, **128**, 153–162.
- Salari M., Konstantinov K. and Liu H.K. (2011). *Journal of Materials Chemistry*, **21**(13), 5128–5133.
- Santara B., Giri P., Dhara S., Imakita K. and Fujii M. (2014). *Journal of Physics D: Applied Physics*, **47**(23).
- Sgroi M., Vagliasindi F.G.A., Snyder S.A. and Roccaro P. (2018). *Chemosphere*, **191**, 685–703.
- Thommes M., Kaneko K., Neimark A.V., Olivier J.P., Rodriguez-Reinoso F., Rouquerol J. and Sing K.S.W. (2015). *Pure and Applied Chemistry*, **87**(9-10), 1051–1069.
- Wang B.S., Hou H. and Gu Y.S. (1999). *Chemical Physics Letters*, **309**(3-4), 274–278.

- Wang S., Wang Z.Y., Wang Y., Xia C.H., Hong E., Bai L.M., Li T. and Wang B.Q. (2019). *Science of the Total Environment*, **652**, 85–92.
- Wang Y.J., Shi R., Lin J. and Zhu Y.F. (2011). *Energy & Environmental Science*, **4**(8), 2922–2929.
- Xing M., Fang W., Nasir M., Ma Y.F., Zhang J.L. and Anpo M. (2013). *Journal of Catalysis*, **297**, 236–243.
- Yang W.X., Ma G.Z., Fu Y., Peng K., Yang H.L., Zhan.X.Q., Yang W.Y., Wang L. and Hou H.L. (2022). *Chemical Engineering Journal*, **429**.
- Yuvakkumar R. and Hong S.J.I. (2015). *Journal of Sol-Gel Science and Technology*, **73**, 511–517.
- Zhang X., Guo Z.R., Sun P.F., Liu X.Y., Luo Z., Li J.Y., Zhang D.X. and Xu X.Y. (2023). *Separation and Purification Technology*, **312**.
- Zhang Z.K., Bai M.L., Guo D.Z., Hou S.M. and Zhang G.M. (2011). *Chemical Communications*, **47**(29), 8439–8441.
- Zhao Z.Y., Liu Q.J. (2008). *Journal of Physics D: Applied Physics*, **41**(8).
- Zhou F. and Ren X. (2020). *Journal of Environmental Science and Health, Part A: Toxic/Hazardous Substances & Environmental Engineering*, **55**(3), 239–255.
- Zhou F., Ren X.H., Qiang H.F., Zeng Y.Z. and Fan M.M. (2021). *Cailiao Gongcheng*, **49**(11), 171–178.
- Zhu Z., Ma C.C., Yu K.S., Lu Z.Y., Liu Z., Huo P.W., Tang X. and Yan Y.S. (2020). *Applied Catalysis, B: Environmental*, **268**.